Dynamics of Atmospheres and Oceans, 5 (1981) 281—306
Elsevier Scientific Publishing Company, Amsterdam — Printed in The Netherlands

THE STABILITY OF BUOYANCY-DRIVEN COASTAL CURRENTS

R.W. GRIFFITHS and P.F. LINDEN

Department of Applied Mathematics and Theoretical Physics, University of Cambridge, Silver Street, Cambridge CB3 9EW (Great Britain)

(Received July 3, 1980; accepted November 14, 1980)

ABSTRACT

Griffiths, R.W. and Linden, P.F., 1981. The stability of buoyancy-driven coastal currents. Dyn. Atmos. Oceans, 5: 281—306.

Buoyancy-driven boundary currents were generated in the laboratory by releasing buoyant fluid from a source adjacent to a vertical boundary in a rotating container. The boundary removed the Coriolis force parallel to it, allowing the buoyant fluid to spread in a current along the boundary. Use of a cylindrical boundary and a line source that released fluid uniformly around the circumference enabled an axisymmetric (zonal) current to be produced. With the continuous release of fluid from the source, the current grew in width and depth until it became unstable to non-axisymmetric disturbances. The wavelength and phase velocities of the disturbances were consistent with a model of baroclinic instability of two-layer flow when frictional dissipation due to Ekman layers is included. However, when the current only occupied a small fraction of the total depth, barotropic processes were also thought to be important, with the growing waves gaining energy from the horizontal shear.

In other experiments, gravity currents were produced by a point source adjacent to either a zonal (circular) or a meridional (radial) vertical boundary. The currents were also observed to become unstable to the same upstream breaking waves as those on the continuous zonal current. Finally, some comparisons are made with oceanic coastal currents.

1. INTRODUCTION

Buoyancy-driven coastal currents occur in many parts of the world oceans. A particularly striking example is the East Greenland Current in which cold, fresh polar water flows southward from the Arctic Ocean along the east coast of Greenland. It occupies a wedge-shaped region some 200 km in width, with the maximum depth (200 m) at the coast. The primary driving force appears to be the density difference between the polar water and the water of the Norwegian Sea. Where land masses are not present, the southward spreading of the less dense polar water is inhibited by the effects of the Earth's rotation. Southward motion induces an east—west flow to conserve angular momentum, and this flow, in turn, produces a north—south Coriolis force which opposes the buoyancy force. Consequently, further southward motion is inhibited. However, at a meridional barrier such as the

0377-0265/81/0000—0000/$02.50

coast of Greenland, the east—west flow and the north—south Coriolis force are removed. Southward motion is therefore possible near the coast, and this flow is accompanied by a Coriolis force directed normal to the boundary. The resulting current hugs the coast line. Such a current was produced by a radial barrier in a laboratory experiment by Wadhams et al. (1979).

There are many other examples of this type of flow. Fresh water entering the ocean from rivers or fjords is often observed to turn to the right (in the Northern Hemisphere) to form a coastal current. On a larger scale, potential density contours show that North Atlantic surface water, after passing through the Straits of Gibraltar into the (more dense) water of the Mediterranean Sea, forms a surface current along the African coast to Tunis. Similarly, the relatively dense water of the Mediterrranean outflow turns north from the Straits of Gibraltar to flow along the Spanish continental shelf. The current flows along the bottom but it is still driven by buoyancy forces and keeps the boundary on its right-hand side.

Satellite photographs of the East Greenland Current are made particularly clear by ice carried from the polar region and they indicate that the flow is unstable. Eddies approximately 50 km in diameter are visible on the edge of the current over its whole length. An example of one of these eddies marked by the ice field is shown in Fig. 12 of Wadhams et al. (1979). These authors also found evidence of patches of warmer water inside the current, possibly due to earlier entrainment by eddies.

In this paper we describe laboratory experiments that examine some of the properties of these buoyancy-driven boundary currents. In particular, the stability of such currents is investigated by observing two types of flow. A uniform current parallel to the boundary was produced by placing a circular (line) source of buoyant fluid around a cylindrical wall. As fluid was continuously supplied to the source, a stable zonal current developed and slowly grew in width until wave-like disturbances appeared. The waves grew in amplitude, broke on the upstream side and formed eddies which had dimensions comparable with the width of the original current. A second type of flow was produced by placing a small confined source at either the cylindrical wall or a straight meridional barrier. The nose of a gravity current then propagated along the boundary. At a point far upstream from the nose the current became sufficiently wide for waves to be unstable, just as on the uniform current. There appear to be no differences between the instabilities on zonal and meridional boundary currents, and such backward-breaking waves have already been seen (Stern, 1980) at the edge of a gravity current on a straight barrier in a rotating system.

The growing disturbances observed in the laboratory system are thought to result from a mixture of barotropic and baroclinic instabilities. The width of the current before instability is always several times larger than the Rossby radius of deformation and, when the depth h of the current is a significant fraction of the total depth H, the disturbances are expected to be predominantly baroclinic. In this case the observed wavelengths are success-

fully predicted by a model for baroclinic instability of a two-layer flow in a staight, rotating channel, when dissipation by Ekman layer suction is included. The critical size of the current is that at which a critical vertical shear is exceeded. When the fractional depth h/H of the current is small (about 10^{-1} or less) the disturbances are probably primarily barotropic, gaining energy from the kinetic energy of the horizontal shear.

Once the disturbances have grown to very large amplitudes, the character of the flow is qualitatively similar to that observed during the instability of isolated baroclinic vortices (Griffiths and Linden, 1981). In particular, we again find pairing of vortices of opposite sign producing modon-like structures.

2. EXPERIMENTAL METHODS

The experiments were carried out on a 1 m diameter, direct-drive turntable, on which was mounted a cylindrical perspex tank (43.5 cm radius, 30 cm deep). The vertical boundary against which most of the currents were generated was a perspex cylinder of radius R_0 = 12.7 cm, placed on the axis of rotation so that flow was confined to an annular region 21.0 cm wide. However, the currents of interest never occupied more than one-half of the width of this region, so the presence of the outer boundary is unimportant.

The tank was filled with a salt solution of density ρ_2 and depth H and brought to solid body rotation. Dyed water of density $\rho_1(<\rho_2)$ was then released from a source placed at the free surface and adjacent to the cylindrical boundary. In most experiments the source consisted of a ring of tubing containing many small holes and covered with plastic foam. This source fitted snugly around the inner cylinder in a horizontal plane, as sketched in Fig. 1, and introduced the buoyant fluid almost uniformly around the whole circumference of the cylinder. The influence of the bottom boundary was investigated by adjusting the initial depth H of the bottom layer. In several experiments an axisymmetric sloping bottom was also placed in the tank, at 10° to the horizontal and extending 16 cm from the

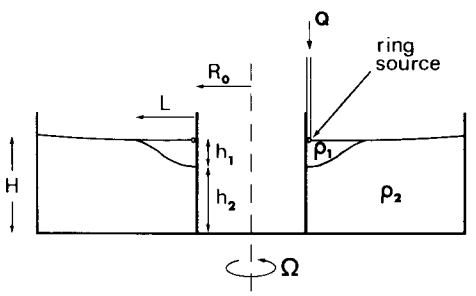

Fig. 1. A definition sketch of the experiment for the line source that surrounds the circumference of the cylindrical wall. The symbols are described in the text and R_0 = 12.7 cm for all experiments.

cylindrical wall. In other experiments the less dense fluid was released from a small source at one point on the boundary. In these experiments we were able to study the nose of the current as it propagated around the cylinder, as well as the stability of the edge of the current well behind the nose. Similar unsteady currents were also produced against a straight, radial barrier. All currents were produced at the free surface to avoid a significant radial loss of fluid in the strong Ekman layers that form at rigid horizontal boundaries.

The buoyancy forces are characterized by the reduced gravitational acceleration $g' = g(\rho_2 - \rho_1)/\rho_1$ between layers. This took values $0.1 \leqslant g' \leqslant 7$ cm s^{-2} while the Coriolis parameter $f = 2\Omega$ was varied throughout $0.5 \leqslant f \leqslant 4$ s^{-1}. H was varied from 3.5 to 28.0 cm. The flow rate Q was monitored by a flowmeter and held constant with the aid of a constant-head device to within 2% during a given experiment. With the circular source the flow rate per unit length lay in the range $0.007 \leqslant Q/2\pi R_0 \leqslant 0.15$ cm^2 s^{-1} while the flow rate from the point source was $1.7 \leqslant Q \leqslant 6$ cm^3 s^{-1}. The kinematic viscosity ν of the fluid remained at 0.01 cm^2 s^{-1}.

The flow was visualized by adding dye and buoyant beads to the source fluid, and recorded by still and movie photography. For plan views the cameras were mounted in the anticlockwise rotating frame of reference. Throughout an experiment the current width L and depths H and h_2 (Fig. 1) were measured directly and also from the photographic record. From the measurements the depth of the upper layer current $h_1 = H - h_2$ and the ratio of layer depths $\gamma = h_1/h_2$ were determined.

3. RING SOURCE EXPERIMENTS

3.1. Stable axisymmetric flow

After leaving the source the fluid is moved radially outward by the buoyancy force. To conserve angular momentum an anticyclonic azimuthal flow is established. The Coriolis force due to this azimuthal flow opposes the radial buoyancy force and equilibrium is reached. The fluid in the environment is of finite depth and must also be displaced radially outward by the growth of the boundary current. Consequently, an anticyclonic azimuthal flow whose magnitude depends upon the ratio of layer depths is produced in the lower layer.

The addition of fluid at a constant rate implies that the depth and width of the upper layer increase as $t^{1/2}$. This behaviour is seen in Fig. 2 where data for dimensionless depth $\hat{h} = f^2 h_1/g'$ and width $\hat{L} = f^2 L/g'$ are plotted as functions of dimensionless time $\hat{t} = Qf^4 t/2\pi R_0 g'^2$ for several experiments. The data deviate slightly from a slope of 1/2 because the scaling does not include any influence of friction or the effect of motion in the environment. Despite this time dependence, at the flow rates used in our experiments the zonal current may be considered to pass through a series of quasi-steady states in which it is always in quasi-geostrophic equilibrium.

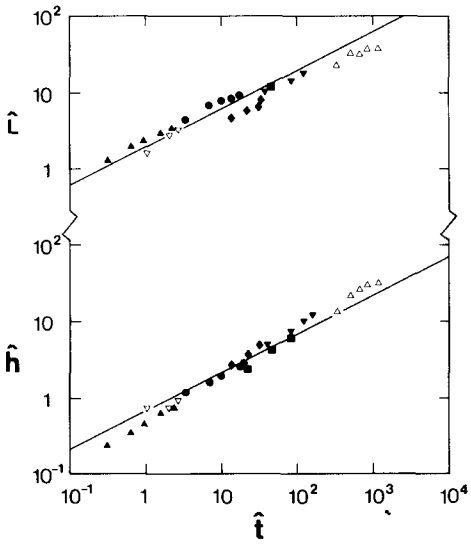

Fig. 2. The non-dimensional width $\hat{L}$ and depth $\hat{h}$ of the axisymmetric current as functions of the non-dimensional time $\hat{t}$. Seven experiments are shown with $0.6 < f < 4.2\ \mathrm{s}^{-1}$, $0.8 < g' < 7.0\ \mathrm{cm\ s}^{-2}$ and $0.04 < Q/2\pi R_0 < 0.13\ \mathrm{cm}^2\ \mathrm{s}^{-1}$. The solid lines have a slope of $\frac{1}{2}$ and have been fitted by eye to the data.

Plan views of two axisymmetric currents are shown in Figs. 3a and 4a, whilst a side view is shown in Fig. 5a. The currents have a maximum depth h_1 at the wall, and their depth decreases smoothly with distance from the wall until the density interface intersects the free surface. This intersection defines the width L of the currents. The details of the depth and velocity profiles in an inviscid system are determined by the conservation of potential vorticity within each layer, while the laboratory flows are also influenced by frictional dissipation. These profiles (and hence those of potential vorticity) cannot be measured with sufficient accuracy to allow direct application of the necessary conditions for barotropic or baroclinic instability (Pedlosky, 1964). However, in every case we observed that wave-like disturbances eventually appeared on the density interface and grew to large amplitude.

3.2. Qualitative aspects of the instability

The most striking characteristic of the unstable flows is the number of waves, n, that appear around the cylindrical boundary. By variation of g' and f (over the ranges given in Section 2) n was varied from 5 to 30. Examples of the onset of instability and the growth of waves are shown in Figs. 3 and 4. These cases gave rise to azimuthal wavenumbers of $n = 6$ and 15 respectively. Instability first appears as small wave-like irregularities on an otherwise axisymmetric current (Figs. 3b and 4b). At this stage the motion is everywhere anticyclonic. However, cyclonic vorticity (initially present near

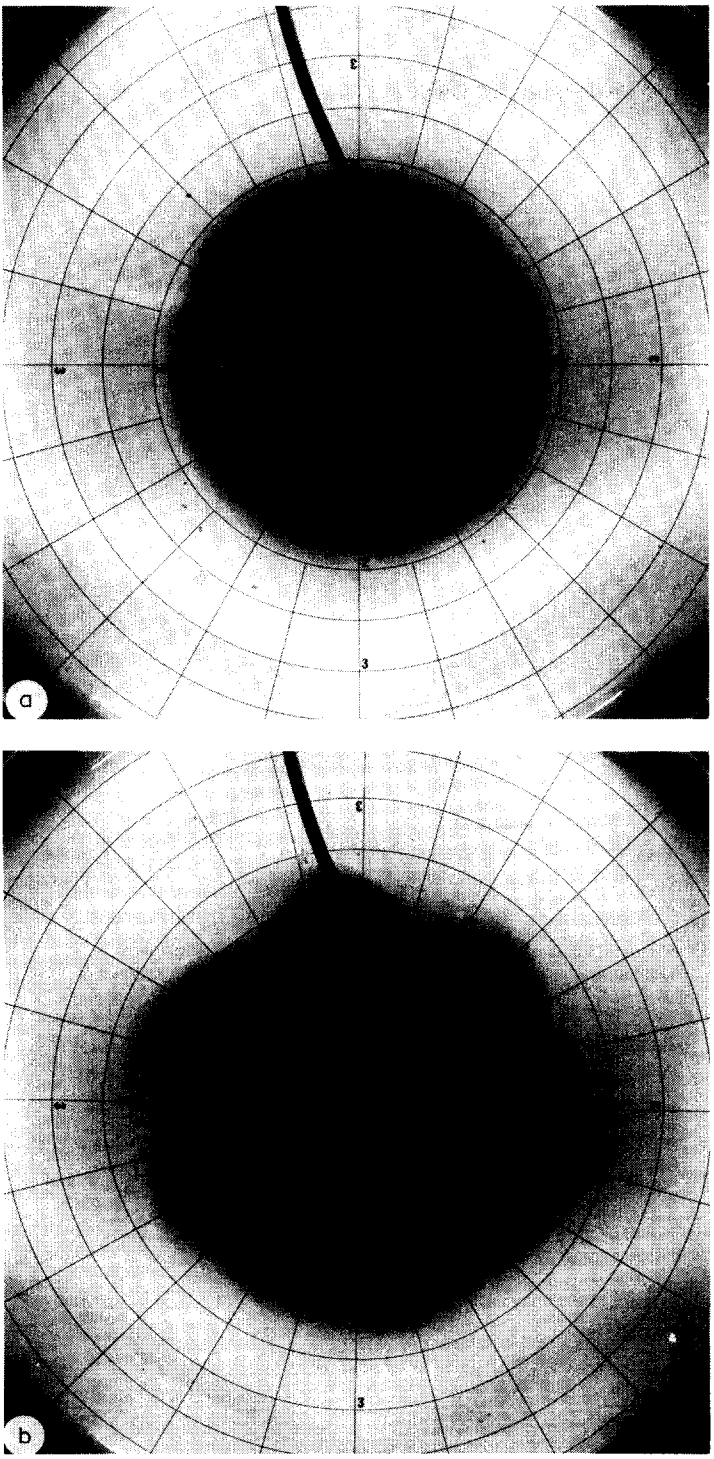

Fig. 3. A sequence of plan view photographs (taken in the rotating frame) showing a current produced by the ring source, which is unstable to a disturbance with azimuthal wavenumber $n = 6$. The photographs were taken at 9(a), 19(b), 23(c) and 28(d) revolutions after the source had been activated. The axisymmetric current is shown in the first frame and the beginning of the growth of disturbances in the second. The subsequent growth of

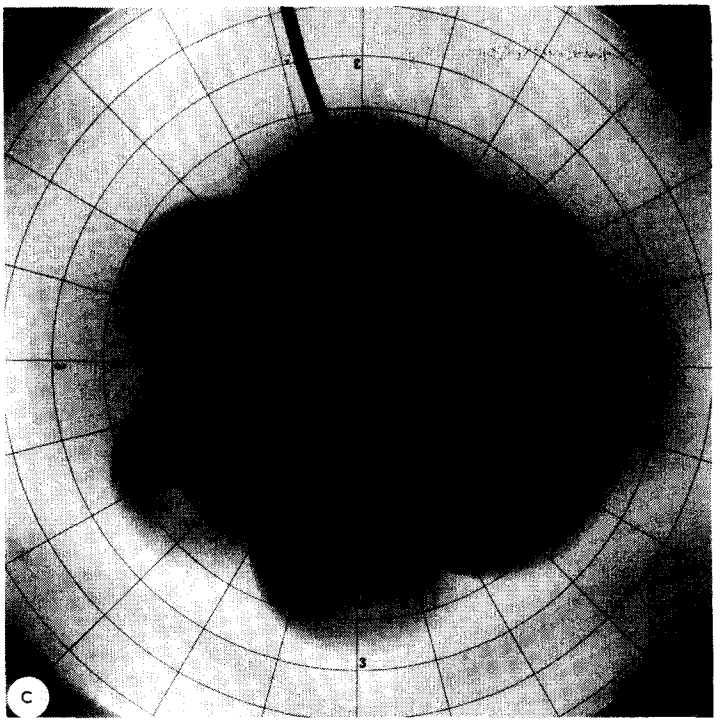

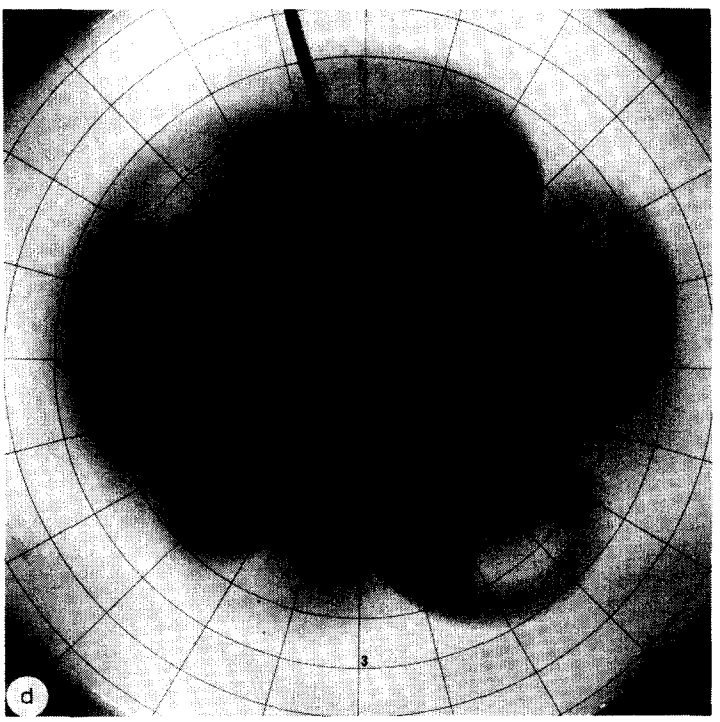

the waves to large amplitude is shown in the third and fourth frames. The direction of rotation is anticlockwise and the current and waves are travelling anticyclonically (i.e. clockwise). Hence the waves appear to break backwards, due to the cyclonic regions produced at the rear of each crest. Concentric circles on the tank bottom are at 5 cm intervals. $f = 1.0\ \mathrm{s}^{-1}$, $g' = 0.85\ \mathrm{cm\ s}^{-2}$, $Q/2\pi R_0 = 0.13\ \mathrm{cm}^2\ \mathrm{s}^{-1}$, $H = 9.9$ cm.

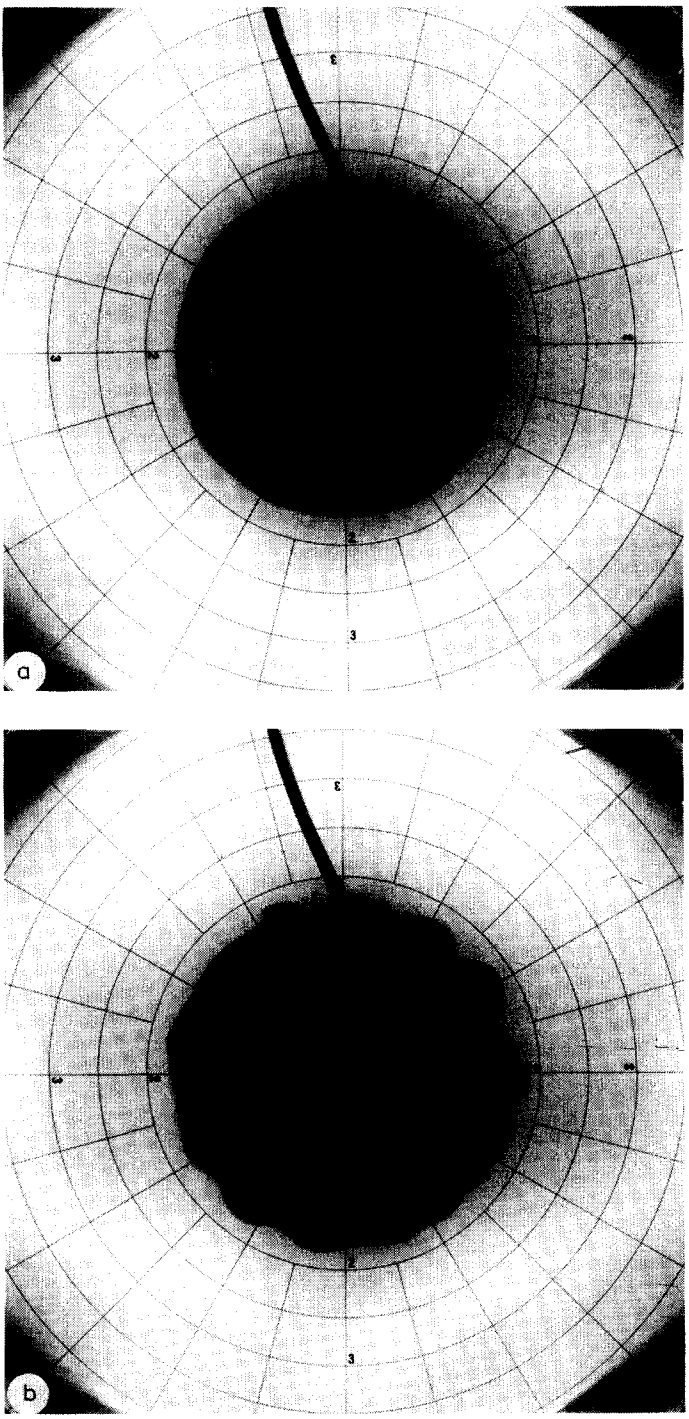

Fig. 4. A similar sequence of plan views to that shown in Fig. 3, except that the current is unstable to a disturbance with azimuthal wavenumber $n \approx 15$. The photographs were

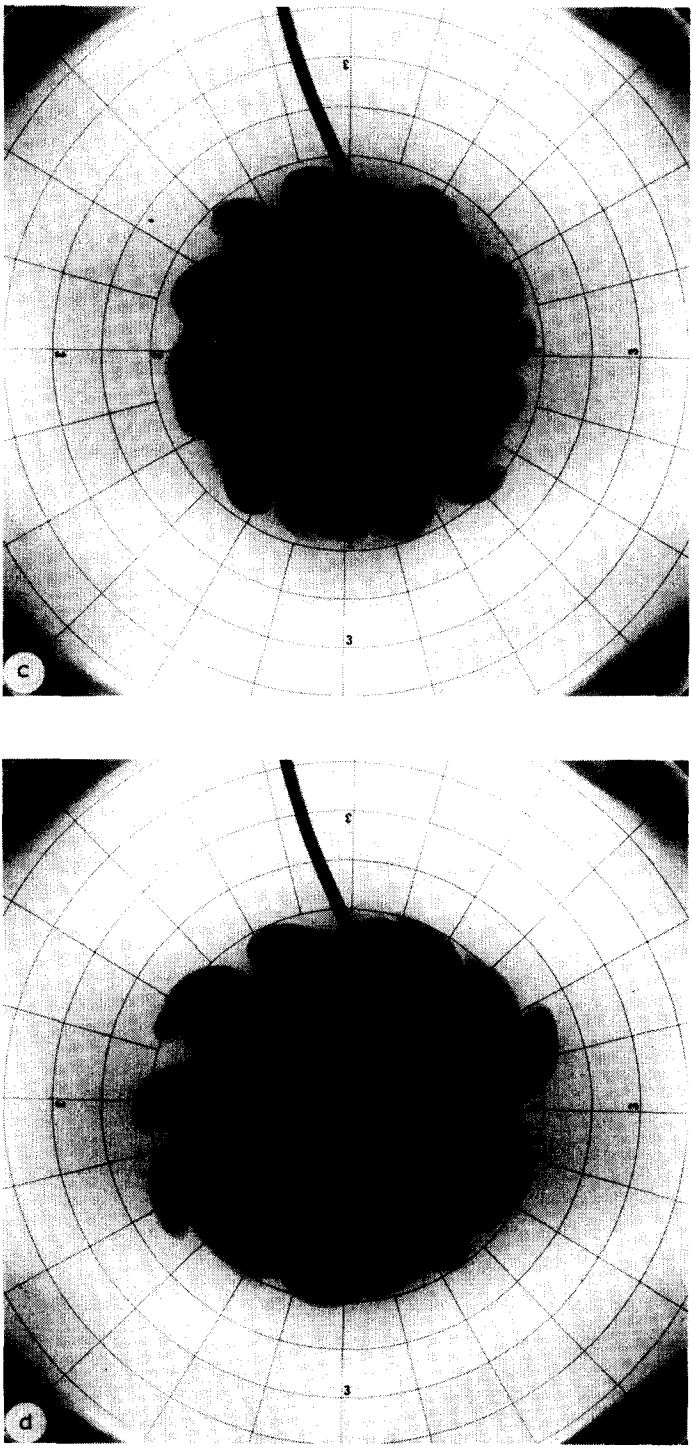

taken at 31(a), 51(b), 58(c) and 67(d) revolutions after the source was activated. f = 3.1 s^{-1}, g' = 0.9 cm s^{-2}, $Q/2\pi R_0$ = 0.04 cm^2 s^{-1}, H = 9.1 cm.

the outer edge of the current) accumulates near the crests of the waves as they continue to grow, and regions of cyclonic motion are eventually produced behind the crests. The cyclonic regions entrain dyed fluid from the waves, giving them the appearance of breaking "backwards" relative to the direction of the current. In Figs. 3c and 4c the flow remains anticyclonic in the current where the dye is darkest but is cyclonic where the dye is thin behind the crests. At this stage the azimuthal variations of the current width and depth are marked. The depth variations can be seen in Fig. 5b, where the deeper sections of the upper layer correspond to the wider, anticyclonic sections near the crests.

The non-axisymmetric flow observed here appears to be very similar to

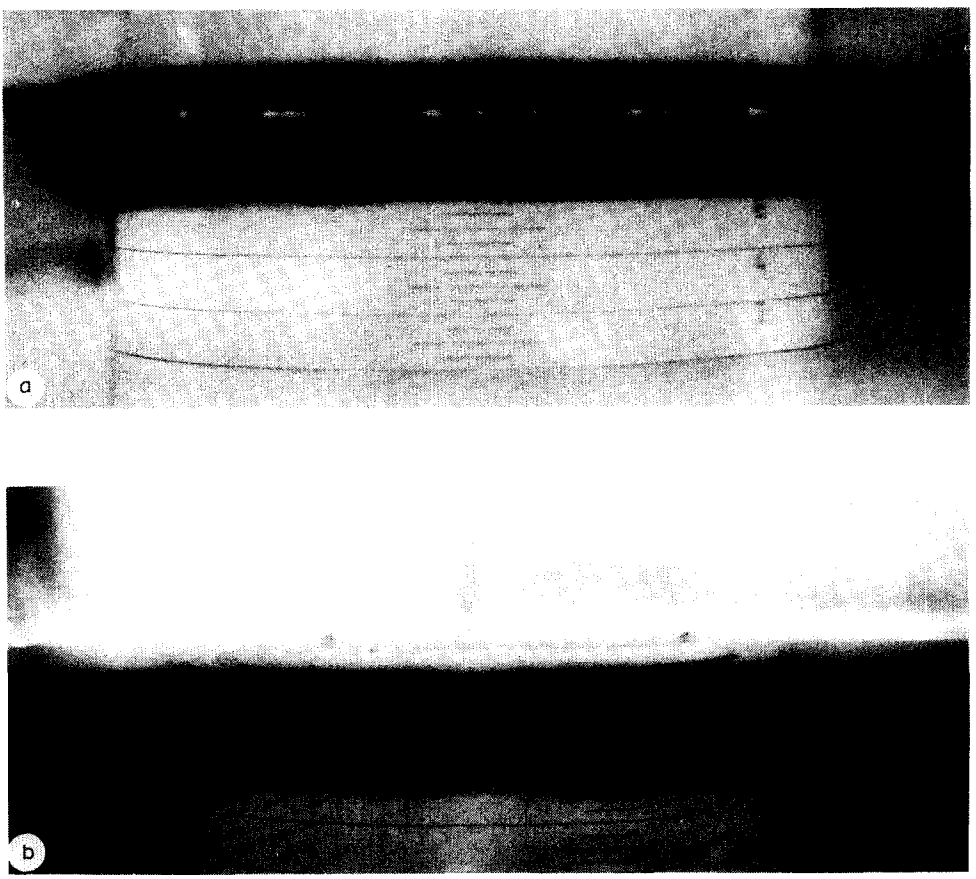

Fig. 5. Side views of the current produced by the ring source. (a) The stable axisymmetric current, showing a smooth profile. (b) The current after the instability has grown to large amplitude. The interface depth now varies quite markedly between the (deep) wave crests and the (shallow) troughs. The scale indicates the depth from the tank bottom in centimetres. The current is reflected in the free surface, which is visible as a bright line.

that which follows the onset of instability of an isolated vortex in a two-layer fluid (Griffiths and Linden, 1981). This similarity is preserved at still greater amplitude (Figs. 3d and 4d). Griffiths and Linden observed the formation of a number of vortex dipoles which caused rapid spreading of buoyant fluid from the initial vortex. In the boundary currents both the anticyclonic motion within the wave crests and the cyclonic motion behind the crests again form closed streamlines. The resultant vortex pairs in these experiments usually did not separate from the wall or from the remaining current. Instead, the non-axisymmetric motions appeared to cease growing when they reached some large amplitude. Only for the very longest waves observed ($n = 5$) did the vortex pairs travel radially away from the wall.

In determining the nature of the boundary current instability, we note that models of baroclinic instability of inviscid two-layer flows on an f plane with no horizontal velocity shear predict that very long waves will be the first to become unstable as the parameter $F = f^2L^2/g'h_1$ is increased past a critical value. For our annular flow the mode $n = 1$ is the longest wave that can be accommodated. On the other hand, the laboratory boundary currents contain horizontal velocity gradients and involve the dissipation of potential vorticity in Ekman layers at the density interface and horizontal boundaries. Both effects (Pedlosky, 1979) are able to stabilize long waves, and both impose a critical value of the vertical shear that must be exceeded before any wavenumbers can grow.

We shall investigate a model for baroclinic instability with friction and an arbitrary ratio of layer depths but with no horizontal shear. The model successfully describes the observed instability. However, because the observed wavelength is always comparable to the width of the current, it cannot be concluded on the basis of these experiments alone that horizontal shear is always unimportant in determining the stability of the current or in selecting the dominant wavenumber.

4. A THEORETICAL MODEL

The stability of an inviscid wedge-shaped boundary current whose outer edge is a density front has been considered for the limit of very long waves by Jones (1977). However, this problem becomes unwieldy when both short waves and the influence of friction are to be studied. Consequently the wedge-shaped boundary current is, for our present purposes, most usefully modelled by a two-layer flow in a straight, infinitely long channel of rectangular cross-section and width L. The density interface is assumed to intersect both vertical walls of the channel instead of forming a front at one edge of the current. The upper and lower layers have depths h_1 and h_2, and velocities U_1 and U_2 parallel to the walls (x direction) respectively. The vertical shear $U_s = U_1 - U_2$ is independent of the normal coordinate y. This problem was first discussed by Phillips (1954), and again by Pedlosky (1970), for the special case in which $h_1 = h_2$. Here we give the essential features of the linear-

ized stability analysis for arbitrary depth ratio when dissipation by Ekman suction is included.

The two-layer system is described by the potential vorticity equations for each layer. With the total geostrophic stream functions in the form $\psi_i = \psi_{i0} + \phi_i(x, y, t)$, $i = 1, 2$, the disturbance stream functions ϕ_i must satisfy the dimensionless equations (Pedlosky, 1970, 1979)

$$\left(\frac{\partial}{\partial t} + U_1 \frac{\partial}{\partial x}\right)[\nabla^2\phi_1 - F_1(\phi_1 - \phi_2)] + F_1 U_S \frac{\partial \phi_1}{\partial x} = \frac{-r_1}{2}\nabla^2\phi_1 \tag{1}$$

$$\left(\frac{\partial}{\partial t} + U_2 \frac{\partial}{\partial x}\right)[\nabla^2\phi_2 - F_2(\phi_2 - \phi_1)] - F_2 U_s \frac{\partial \phi_2}{\partial x} = \frac{-r_2}{2}\nabla^2\phi_2 \tag{2}$$

where

$$r_1 = (2E_1)^{1/2}/\epsilon_1 , \quad r_2 = (2E_2)^{1/2}/\epsilon_2$$

and the Froude numbers are defined as

$$F_1 = f^2L^2/g'h_1 , \quad F_2 = f^2L^2/g'h_2$$

The friction parameters for each layer depend upon the individual Ekman numbers $E_i = \nu/h_i^2 f$ and Rossby numbers $\epsilon_i = u_i/fL$, where u_i are velocity scales. Then

$$r_1 = \frac{(2\nu f)^{1/2}}{u_1}\frac{L}{h_1} , \quad r_2 = \frac{(2\nu f)^{1/2}}{u_2}\frac{L}{h_2} \tag{3}$$

These equations only correctly describe the friction due to rigid horizontal boundaries, but should give a reasonable description of the effects of interfacial Ekman layers.

A disturbance of the form

$$\phi_i = A_i \exp[ik(x - ct)] \cos ly$$

must satisfy the condition of no normal flow ($\phi_i = 0$) at $y = \pm 1/2$. Then the cross-stream wavenumber is $l = (2j + 1)\pi$, $j = 0, 1, 2, \ldots$ and the horizontal wavenumber K is given by $K^2 = k^2 + l^2$. Substitution of this perturbation into (1) and (2) yields

$$-a_1[(c - U_1)(K^2 + F_1) + F_1U_s - r_1K^2/2ik] + a_2(c - U_1)F_1 = 0$$

$$a_1(c - U_2)F_2 - a_2[(c - U_2)(K^2 + F_2) - F_2U_s - r_2K^2/2ik] = 0$$

from which the complex value of $c = c_r + ic_i$ is found to satisfy

$$\alpha c^2 + \beta c + \Gamma = 0 \tag{4}$$

where

$$\alpha = K^2(K^2 + F_1 + F_2)$$

$$\beta = -(U_1 + U_2)\,K^2(K^2 + F_1 + F_2) + U_s K^2(F_1 - F_2)$$

$$+ (iK^2/2k)[(K^2 + F_1)\,r_1 + (K^2 + F_2)\,r_2]$$

$$\Gamma = K^2(K^2 U_1 U_2 + U_1^2 F_2 + U_2^2 F_1) - (r_1 r_2/4)\,K^4/k^2$$

$$- (iK^2/2k)[(K^2 U_2 + F_2 U_1)\,r_1 + (K^2 U_1 + F_1 U_2)\,r_2]\,.$$

Marginally stable conditions ($c_i = 0$) occur when

$$\frac{k^2 U_s^2}{r_1 r_2} = \frac{[(K^2 + F_1)(K^2 + F_2) - F_1 F_2]\,S}{(K^4 - 2F_1F_2)^2(r_2 - r_1)^2 - (K^4 - 4F_1F_2)\,S} \tag{5}$$

where

$$S = (K^2 + F_2)^2 r_2^2 + (K^2 + F_1)^2 r_1^2 + 2(K^2 + F_1)(K^2 + F_2)\,r_1 r_2$$

At this stage it is convenient to restrict attention to the case in which the Ekman layers in the upper layer are identical to those in the lower layer, so that

$$r_2/r_1 = h_1/h_2 \tag{6}$$

This will be so when both top and bottom boundaries are identical, or when dissipation within each layer is dominated by the interfacial Ekman layers. This assumption should be reasonable for $h_1 \ll h_2$, when the influence of bottom friction on the deep lower layer is small compared with the effect of interfacial friction on the upper layer. For $h_1 \approx h_2$ the assumption should preserve at least the qualitative effects of friction in the laboratory system, which has a free upper surface, a sharp density interface and a rigid lower boundary.

The depth ratio is defined as $\gamma = h_1/h_2$ ($=(H - h_2)/h_2$) and we write

$$r_2 = \gamma r_1\,, \quad F_2 = \gamma F_1 \tag{7}$$

in (5) to obtain

$$\left(\frac{U_s}{r_1}\right)^2 \frac{1}{\gamma} = \frac{K^2(K^2 + F_1 + \gamma F_1)}{(K^2 - l^2)\,[(K^4 - 2\gamma F_1^2)^2(\gamma - 1)^2 - (K^4 - 4\gamma F_1^2)\,\sigma]} \tag{8}$$

with

$$\sigma = (K^2 + \gamma F_1)^2 + \gamma^2(K^2 + F_1)^2 + 2\gamma(K^2 + F_1)(K^2 + \gamma F_1)$$

The special case in which the layers have equal depths has been discussed in detail elsewhere (e.g. Pedlosky, 1979). When $\gamma = 1$, (8) reduces to

$$U_s/r_1 = K(K^2 - l^2)^{-1/2}(2F_1 - K^2)^{-1/2} \tag{9}$$

from which it can be seen that the gravest cross-stream mode ($l = \pi$) is the most unstable. For all values of the vertical shear, both long waves with $K^2 = l^2$ (i.e. $k = 0$) and short waves with $K^2 > 2F_1$ are stable. This short-wave cut-

off is the same as that found for the inviscid problem, but in that problem there is no long-wave cut-off and no critical shear that must be exceeded. For a given vertical shear U_s, (9) implies that all wavenumbers are stable unless $F_1 > l^2/2$. At a given value of $F_1 > l^2/2$ there is also a minimum shear U_c that must be exceeded before any wavenumbers can grow. The minimum of (9) occurs at $K_m = (2l^2F_1)^{1/2}$, which is the first mode to become unstable as the vertical shear is increased beyond U_c. The most unstable wavelength is then

$$2\pi/k_m = 2\pi F_1^{-1/4}/(2^{1/2}l - l^2F_1^{-1/2})^{1/2} \tag{10}$$

and the critical shear is

$$U_c = r_1/[(2F_1)^{1/2} - l] \tag{11}$$

The phase speed of the small-amplitude unstable mode when $\gamma = 1$ is $c_r = (U_1 + U_2)/2$. These waves are advected downstream despite having a propagation velocity that is upstream relative to the upper layer motion.

Before discussion of the marginally stable modes for more general values of γ, a simple transformation will allow our channel model to describe more accurately the boundary current of which one edge is a density front instead of a rigid wall. In that case the amplitude of disturbances is largest at the current edge and zero at the boundary. Therefore, the cross-stream wavenumber should be redefined as though the channel were of width $2L$. Then $l = (j + \frac{1}{2})\pi$, $j = 0, 1, 2, \ldots$. This change does not alter the theory above and does not accurately describe the effects of the wedge shape currents in which $h_1 \to 0$ at the front. The deepest cross-stream mode becomes that with $l = \pi/2$, a value that will be assumed throughout the following discussion. From (9) the critical value of the Froude number F_1 below which all wavenumbers are stable at all values of U_s is then $\pi^2/8$.

The marginally stable modes given by (8) for more general values of γ are plotted in Fig. 6 for $F_1 = 10$. The behaviour is qualitatively unchanged at other values of F_1. In constrast to the inviscid flow where all wavenumbers $K^2 < 2F_1$ are unstable, there is also a long-wave cut-off beyond which the waves are stabilized by viscous dissipation. For each value of γ the curve of marginal stability has a minium at $K_m^2 = k_m^2 + l^2$, and therefore waves with the (finite) wavelength $\lambda = 2\pi L/k_m$ are the first to become unstable as the vertical shear is increased. This wavelength does not vary rapidly with γ.

As γ decreases, the long-wave cut-off remains at $K^2 = l^2$ but the range of unstable wavenumbers diminishes because the short-wave cut-off occurs at decreasing values of K. U_c increases more rapidly than $\gamma^{-3/2}$ as γ becomes small, and becomes infinite at small (but finite) γ. This is where the long- and short-wave cut-offs coalesce. Below this value of γ the current is always stable to baroclinic disturbances.

The value of γ at which the critical shear becomes infinite depends on F_1. Thus, for any given γ there is a critical upper-layer Froude number F_c below which the flow is stable to all baroclinic disturbances. The value of F_c is

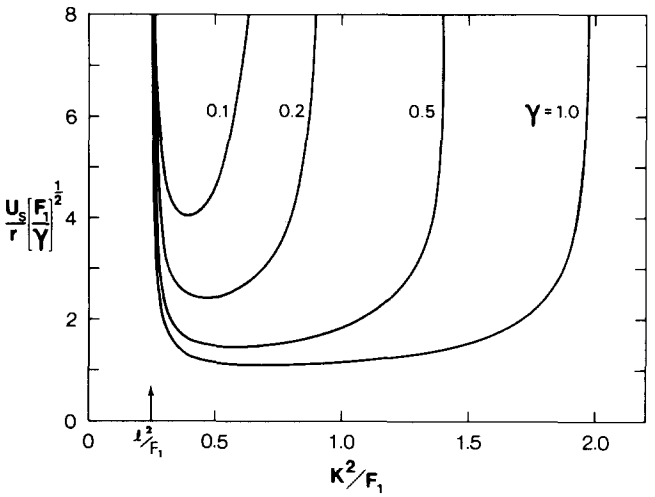

Fig. 6. Marginally stable conditions calculated from (8) (with $l = \pi/2$) for $F_1 = 10$ and $\gamma = 1, 0.5, 0.2$ and 0.1. At each depth ratio a range of wavenumbers K are unstable when the vertical shear U_s exceeds a minimum critical value. For this value of F_1 the long- and short-wave cut-offs coalesce at $\gamma = 0.007$. Hence there is absolute stability at all values of the vertical shear when $\gamma < 0.007$.

found by setting the term in square brackets in the denominator of (8) to zero at $K = l$, and is plotted against γ in Fig. 7. If γ and the vertical shear are held fixed while F_1 is increased from a value below the line in Fig. 7, instability occurs at $F_1 > F_c$ (since some waves with $K^2 < 2F_1$ are stabilized by friction). Very long waves are the first to grow in this case.

The critical Froude number F_c that is given by the above model is almost identical to that found for wedge-shaped boundary currents whose outer

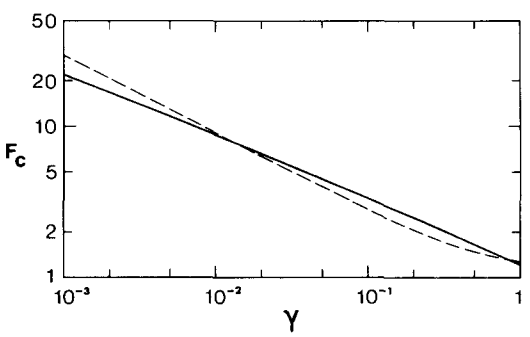

Fig. 7. The critical Froude number F_c as a function of the depth ratio $\gamma = h_1/h_2$, below which all wavenumbers are stable at any vertical shear. The solid line is given by the present model with finite channel width, and the broken line by calculations for a more realistic wedge-shaped current with a uniform velocity and a free front (Jones, 1977).

edge is a front in an infinitely wide channel. Jones (1977) considered very long waves on such a current for uniform velocity U_1 (thus only baroclinic instability was allowed), and found those critical Froude numbers shown by the broken line in Fig. 7. The depths h_1 and h_2 are now the layer depths at the wall and $\gamma = h_1/h_2$ as before. In the Phillips model the interface slope is assumed to be small and therefore the dependence of the results on γ is symmetric about $\gamma = 1$. However, the wedge shape of the current considered by Jones causes different behaviours for $\gamma < 1$ and $\gamma > 1$. He found that the critical Froude number reaches a minimum value $F_c = 1.23$ at $\gamma = 2$ (where the mean depths of the two layers are equal), and approaches the limit $F_c = 2$ at $\gamma \to \infty$ (where the upper layer reaches the bottom at the wall). At the opposite extreme F_c increases with decreasing depth ratio according to $F_c \approx 0.95\,\gamma^{-1/2}$ at $\gamma << 1$. For comparison the Phillips model predicts that $F_c = 1.23$ at $\gamma = 1$ and $F_c \approx 1.2\,\gamma^{-0.42}$ at $\gamma << 1$. Thus the shape of the density interface and the presence or absence of a rigid vertical wall at a distance $2L$ from the boundary (a distance L beyond the front) have little influence upon the conditions for absolute stability to long waves.

5. COMPARISON OF MODEL AND EXPERIMENTAL RESULTS

Measurements of the current width L and depth h (some of which are presented in Fig. 2) show that, during the axisymmetric phase of the flow, the Froude number increases with time. Indeed, $F_1 \propto t^{1/2}$ to a reasonable approximation. For all experiments, $0.07 \leq \gamma \leq 1$ and the corresponding theoretical critical Froude numbers F_c are as shown in Fig. 7. The measurements also reveal that, in all experiments, F_1 is significantly greater than F_c

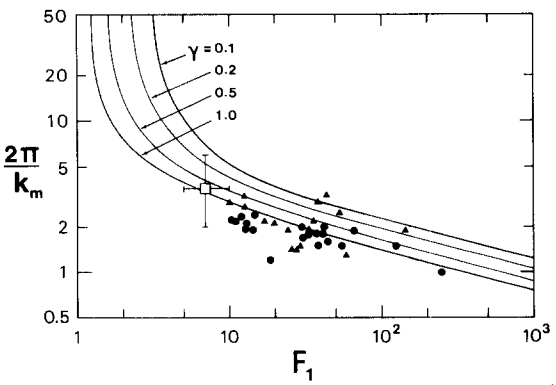

Fig. 8. The dimensionless wavelength $2\pi/k_m = \lambda/L^*$ as a function of the Froude number $F_1 = f^2L^{*2}/g'h_1^*$. The data are plotted on coordinates calculated from L^* and h_1^* (width and depth of current) measured just before instability and from $\lambda = 2\pi R_0/n$. ▲ $\gamma < 0.25$, ● $\gamma > 0.25$. The curves show the most unstable wavelengths (obtained by finding the minimum of (8) with $l = \pi/2$) at a given value of γ. The square represents all observations of the conditions at which waves appear on gravity currents produced by a continuous flux from a point source (against either circular or radial barriers).

very soon (about 30 s) after the source is activated and that growing disturbances first become visible at a Froude number $F_1 >> F_c$. At the same time, the velocity difference U_s between the layers must increase as the current width and depth increase. Furthermore, the critical shear decreases as F_1 increases. These observations suggest that, if the instability is baroclinic, marginally stable conditions are reached only when the vertical shear becomes sufficiently large (Fig. 6).

The observed dimensionless wavelengths λ/L^* of the growing disturbances are plotted against the Froude number $F_1^* = f^2L^{*2}/g'h_1^*$ in Fig. 8, where L^* and h_1^* are the width and depth of the current measured immediately prior to the appearance of the growing disturbances. The wavelength λ, or the zonal wavenumber k_m, is calculated from the azimuthal wavenumber n and the cylinder radius R_0 according to

$$\lambda/L^* \equiv 2\pi/k_m = 2\pi R_0/L^*n \tag{12}$$

The results have been arbitrarily divided according to $\gamma < 0.25$ (triangles) and $\gamma > 0.25$ (circles). The curves show the wavelengths of the marginally stable modes as predicted by (8) for four depth ratios. The model implies that $k_m \to 0$ when $F_1 \to F_c$ while $k_m \approx F_1^{1/4}$ when $F_1 >> F_c$.

The observed wavelengths are equal to those predicted for baroclinic instability to well within the scatter of the data. * There are significant experimental uncertainties that could produce the observed scatter. Each measurement of L and h_1 has a possible systematic error of at least 10%, while $\lambda = 2\pi R_0/n$ may differ from the true wavelength for two reasons. Firstly, the current has a finite width (2—10 cm) so that $2\pi R_0$ may underestimate its effective length. Secondly, the periodicity of the circular system implies that λ may be shifted from that predicted in the infinite channel by up to 2% at $n = 20$ and 10% at $n = 5$.

The data in Fig. 8 shows that the dimensionless wavelength is almost constant at $\lambda/L^* \approx 2$, despite a large variation in n. The waves are longer when the current at the onset of instability is wider (L^*n in eq. 12 is almost constant). From the values of $F_1^* = f^2L^{*2}/g'h_1^*$ in Fig. 8 we see that $F_1^* >> 1$ in all the experiments. Consequently, the current width at the onset of instability and the wavelength λ of the dominant disturbance are at least several times the Rossby radius of deformation of the upper layer $(g'h_1^*)^{1/2}/f$. In fact, $6 < f\lambda/(g'h^*)^{1/2} < 30$.

Instability in a two-layer flow is likely to be predominantly baroclinic when $L >> (g'h_1)^{1/2}/f$ and γ is not too small (e.g. Killworth, 1980; Holland and Haidvogel, 1980). Thus the result that the observed wavelength is $\lambda > 6(g'h^*)^{1/2}/f$ is consistent with the quasi-steady approach of the current to marginally unstable (baroclinic) conditions ($U_s \approx U_c$ at $F_1 > F_c$). In contrast,

* Note added in proof: The fit between the data and the theoretical model is even better if the Froude number is based on the mean depth of the upper layer, rather than on h_1, the maximum depth at the wall.

a shorter length scale $g'^{1/2}(h_1^* h_2^*)^{1/4}/f = \gamma^{1/4}(g' h_1^*)^{1/2}/f$ is expected to appear when baroclinic instability occurs at supercritical conditions (Griffiths and Linden, 1981; Killworth, 1980).

On the other hand, previous studies of mixed barotropic instabilities have indicated that the horizontal shear may become an important source of kinetic energy for the small-amplitude disturbances when the ratio of layer depths is sufficiently small. For isolated vortices, with $L > (g' h_1)^{1/2} f^{-1}$, Griffiths and Linden (1981) have shown that barotropic processes significantly influence the wavelength of the dominant growing mode when $\gamma < 10^{-1}$. As has been shown both experimentally (Hide, 1967) and theoretically (Busse, 1968) the scale of the observed barotropic mode is comparable with the thickness of the shear layer. In our experiments horizontal shear exists across the whole current width L. Consequently, the observation that $\lambda \approx 2L^*$ is also consistent with the expected wavelength of a barotropic instability.

A possible way to determine the nature of the instability is to observe the dependence of the critical conditions for instability, and of the subsequent length scales of the flow, upon the ratio of layer depths. However, the data of Fig. 8 reveal almost no variation of the dominant wavelength upon the depth ratio, and no systematic relationship between γ and the Froude number at instability. Considering the scatter of the data, this result is consistent with the model of baroclinic instability and so yields no information about the real importance of the presence of the bottom boundary.

When the sloping bottom was used, though, a small but significant variation of wavenumber (from $n = 10$ to 12 at $\gamma \approx 1$ for example) was observed. Instability (in this example) occurred when the current was 5 cm wide and the sloping bottom was responsible for a 30% variation of the total fluid depth H over the current width. For the smaller depth ratios the sloping bottom produced a much smaller fractional variation of the fluid depth, and no influence upon the flow was evident. We conclude, therefore, that a two-layer baroclinic mechanism selects the dominant wavelength at least at depth

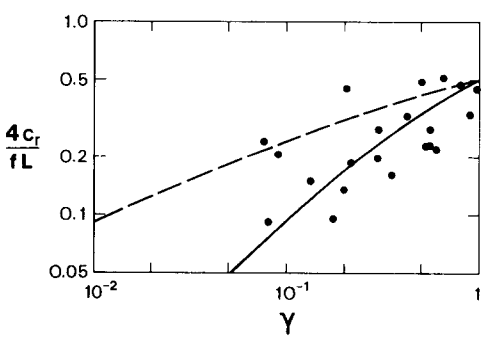

Fig. 9. The (anticyclonic) phase speed of the waves, non-dimensionalized by the velocity scale $fL/4$ of the current, plotted against the depth ratio $\gamma = h_1/h_2$. The solid line is the predicted phase speed for long waves (eq. 14), and the broken line that for the shortest possible waves (eq. 15).

ratios close to one. At small depth ratios ($\gamma \approx 10^{-1}$) we cannot determine empirically which of the two instability mechanisms is dominant, but previous studies suggest that baroclinic instability is still important.

During the growth of the disturbances the wave pattern was observed to drift anticyclonically. By timing the passage of a wave crest through a 30° sector the phase velocity c_r of the waves was determined. The results of these measurements are shown in Fig. 9 where the non-dimensional phase speed $4c_r/fL$ has been plotted against γ. The phase speed has been non-dimensionalized by the velocity scale $fL/4$ which roughly corresponds to the mean velocity $\Omega L/2$ of the upper layer, where $\Omega = f/2$.

If the fluid is inviscid then the model discussed in Section 4 yields an exact expression for the phase speed

$$c_r = [U_1(K^2 + 2F_2) + U_2(K^2 + 2F_1)]/2(K^2 + F_1 + F_2) \tag{13}$$

For long waves, $K^2 << F_1$, F_2 and (13) reduces to

$$c_r \approx (\gamma U_1 + U_2)/(1 + \gamma) \tag{14}$$

whilst at the short-wave cut-off $K^2 = 2(F_1F_2)^{1/2}$ and

$$c_r = (\gamma^{1/2}U_1 + U_2)/(1 + \gamma^{1/2}) \,. \tag{15}$$

When the layer depths are equal (14) and (15) give a phase speed equal to the mean of U_1 and U_2.

Curves (14) and (15), with $U_1 = fL/4$ and $U_2 = 0$, are plotted in Fig. 9. The curve (14) for long waves describes the data reasonably well, whereas the observed phase speed is generally less than that corresponding to the shortest possible waves (eq. 15). This is consistent with the fact that in the presence of frictional dissipation the wavenumber of the marginally stable mode is quite close to the long-wave cut-off (Fig. 6). The waves travel downstream, although at a speed considerably less than the speed of the current. Thus, relative to an observer moving with the upper layer current, the waves propagate upstream.

6. POINT SOURCE EXPERIMENTS

In a number of experiments, less dense fluid was emitted from a "point" source placed at the free surface and adjacent to a vertical boundary. Two different boundaries were used: either the cylinder that was used for the line source experiments or a straight vertical wall. The cylindrical wall was always concentric with the rotation axis, forming a zonal boundary, whilst the straight wall lay along a diameter of the turntable, forming a meridional boundary. The source was surrounded on three sides by a small rectangular box so that the fluid entering the current was initially constrained to flow parallel to the boundary.

In both set-ups fluid from the source formed a narrow current along the boundary, keeping the barrier on its right. At the front of the advancing

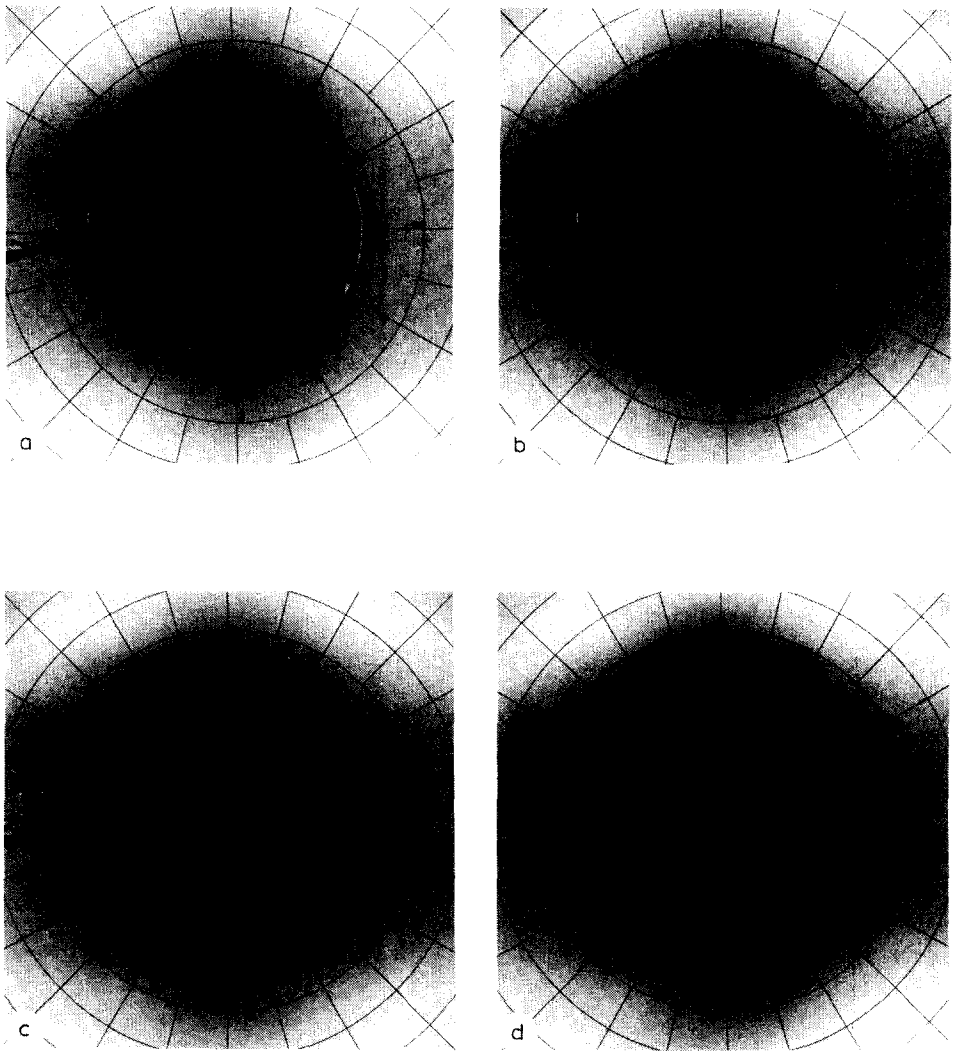

Fig. 10. A sequence of plan view photographs showing the anticyclonic boundary current generated from a point source adjacent to a cylindrical boundary. The photographs were taken 45 (a), 68 (b), 91 (c) and 117 s (d) after the source was activated. The early stage in the growth of a disturbance is visible approximately 30° downstream of the source in (a). In (b) this wave has travelled around to 50° and a new instability is growing at 30° from the source. Other waves begin to develop as is shown on (c) and (d). As on the current generated by the ring source, the waves travel downstream (anticyclonically) and break backwards. $f = 3.0\ s^{-1}$, $g' = 0.75\ cm\ s^{-2}$, $Q = 2.3\ cm^3\ s^{-1}$, $H = 8.7$ cm.

gravity current (the nose) the width and depth of the upper layer decreased smoothly to zero. The foremost part of the nose was immediately adjacent to the boundary. We have not made a systematic study of the properties of the nose (e.g. its propagation velocity), but have instead concentrated on the flow well behind the nose.

As an example of this flow Fig. 10 shows a sequence of plan views of a current as it moves around a cylindrical boundary: waves form on the current and appear to be identical to those observed on the continuous currents described in Section 3. Cyclonic regions are again formed at the rear of the wave crests; these regions contain fluid from the current, giving the waves the appearance of breaking backwards. The waves again move in the direction of flow, but more slowly than the current.

Away from the immediate vicinity of the source, the depth and width of the current decrease with increasing distance downstream. At any point on the boundary the depth and width of the current increase with time and the width is always from one to three times the Rossby radius of deformation. The first wave appears at a point not far from the source (Fig. 10b), where the width and depth, and consequently the Froude number $F_1 = f^2L^2/g'h_1$, are largest. The ratio of layer depths is also greatest near the source and in these experiments it was always in the range $0.2 \leqslant \gamma \leqslant 0.4$. The Froude number near the point at which the first wave was seen is always slightly greater than the critical value (Fig. 7), taking values $5 \leqslant F_1^* \leqslant 10$. There was no dependence of F_1^* upon the type of boundary used. Waves were later observed to grow at other positions along the current.

Although it was difficult to make accurate measurements of the wavelength λ that first appeared, it was in the range $3 < \lambda/L^* < 6$. This result is plotted in Fig. 8 (square) and is consistent with the baroclinic instability model presented in Section 4. However, the currents produced by a point source of buoyant fluid became unstable at smaller Froude numbers than did the currents produced by a zonally independent source. This difference is probably due to a larger current velocity in the point source experiments, produced by an additional (buoyancy-induced) pressure gradient parallel to the boundary. The axisymmetric current produced by a ring source, on the other hand, is driven entirely by the need to conserve potential vorticity as the fluid spreads radially. Thus the critical shear required for instability is probably exceeded at a smaller current width and a smaller F_1 in the point source experiments. We conclude that there is no essential difference between the waves observed on the continuous current and those on the current of finite length. There is also no detectable difference between the zonal and meridional currents.

7. DISCUSSION AND CONCLUSIONS

Boundary currents in a two-layer rotating system that are driven by their own buoyancy were produced in a laboratory tank. Buoyant fluid is supplied continuously from a source, and the currents increase in width and depth to a size at which they become unstable to wave-like disturbances. The ob-observed wavelength is consistent with that of the most unstable mode predicted by a simple model for baroclinic instability of the boundary current. The influence of viscous dissipation, via Ekman layer suction, is important

and it stabilizes long waves. The Froude number $F_1 = f^2L^2/g'h_1$ is always greater than the inviscid critical value at the appropriate ratio of layer depths, $\gamma = h_1/h_2$. In many cases instability does not occur until $F_1 \approx 60F_c$, where F_c is the critical Froude number above which some waves are unstable if the vertical shear is infinitely large. It is concluded that each current, whether infinitely long (around a circular boundary) or of finite length, becomes unstable when it reaches a width at which a critical value of the velocity difference between the layers is exceeded.

There appear to be no significant differences between the unstable waves that appear on boundary currents propagating along either zonal (circular) or meridional (radial) barriers. In all cases the waves travel downstream relative to a fixed point on the boundary. The phase velocity of the waves is smaller than that of the current and so, to an observer moving with the current, they appear to propagate upstream.

The laboratory currents involve a horizontal shear that is not included in the theoretical model, and the ratio of the layer depths is sometimes as small as $\gamma \approx 10^{-1}$. Therefore disturbances in some experiments might extract energy from the kinetic energy of the basic flow. If this mechanism is dominant over that releasing potential energy, the most unstable wavelength will be of the order of the current width. Since this wavelength is consistent with both the observed wavelengths and those predicted for baroclinic instability, we cannot empirically determine which mechanism is important in a given experiment unless we have more information about the importance of the lower boundary. However, our model for the onset of baroclinic instability in the presence of Ekman layer dissipation predicts no greater variation of wavelength with depth ratio than is consistent with the scatter of the data. The addition of a sloping bottom, though, does decrease the observed wavelength at depth ratios close to one, implying that the baroclinic mechanism selects the dominant length scale. At smaller depth ratios we can only infer from other studies (Killworth, 1980; Griffiths and Linden, 1981) that baroclinic instability is still important.

At large amplitude the waves appear to break on the upstream side, and form closed anticyclonic circulations within the wave crests and cyclonic regions behind each crest. However, these vortex pairs are not observed to move away from the boundary. Instead, the non-axisymmetric motions grow until they reach a large and almost stationary amplitude. This behaviour is consistent with models of finite-amplitude baroclinic instability (Pedlosky, 1970), in which friction restricts waves to grow monotonically towards a constant amplitude. The final boundary current has a diffuse nature with large spatial variations of fluid density and velocity.

The stability of the axisymmetric zonal boundary currents may be compared to that of isolated circular vortices in a two-layer system. For baroclinic vortices produced by a constant flux of buoyant fluid from a point source, Griffiths and Linden (1981) found that a vortex grows in radius and depth until the parameter $\theta\gamma^{-1/2}$ decreases beyond a critical value (about

0.02). Here, $\theta = g'h_1/f^2R^2$ and R is the vortex radius. At this point the vortex becomes unstable to non-axisymmetric disturbances with azimuthal wavenumber $n = 2$. This is consistent with models of baroclinic instability in an inviscid fluid, which predict that very long waves are the first to become unstable as $\theta\gamma^{-1/2}$ becomes smaller than a critical value (or order one). The mode $n = 2$ is the longest wave that can release potential energy from a circular vortex at the free surface. To compare this result with those for the boundary currents we note that for the vortices $\lambda/R = 2\pi/n$ (where n must be an integer) and $\theta = F_1^{-1}$. The observed values are $\lambda/R^* = \pi$ and $F_1 \approx 50$, and this point lies well within the scatter of the wavelengths observed on the boundary currents (Fig. 8).

The baroclinic instability model with frictional dissipation, on the other hand, would lead us to expect from the values of F_1 and γ measured at instability that the vortices would give rise to modes with either $n = 2$ ($\lambda/R^* \approx 3$) at small depth ratios or $n = 3$ ($\lambda/R^* \approx 2$) at $\gamma \approx 1$. The vortex should grow in time (at a fixed F_1) until both γ and the vertical velocity shear become large enough for modes with $n \geqslant 2$ to become unstable. Thus friction will not stabilize the $n = 2$ modes for the vortices, even though it is able to stabilize modes with azimuthal wavenumbers $n >> 2$ for the boundary currents.

Another class of waves has been predicted to be possible on the outer edge of a coastal gravity current. For fluids with zero potential vorticity Stern (1980) showed that, if the current width far upstream of the nose is less than a critical fraction (0.42) of the Rossby radius of deformation (based on the current depth far upstream), then the nose of the current will propagate along the coast as a bore. The form of the nose may be steady if friction is able to dissipate sufficient kinetic energy. If the upstream current is wider than this critical value the bore solution does not exist, and the flow may be blocked and diverted perpendicular to the coast. Alternatively, wedge-like solutions, in which the nose of the gravity current travels faster than the flow behind it, are possible when the upstream width is less than $2^{1/2}$ times the Rossby radius. This is also the maximum possible width for an infinitely long, geostrophic current with zero potential vorticity, that forms a unidirectional flow parallel to the boundary. At this critical width ($F_1 = 2$) the equations of motion admit long, non-linear, quasi-geostrophic waves that steepen on one side. This suggests that breaking waves may be observed. However, it is not clear when these waves will grow.

In our experiments the currents produced by a point source of buoyant fluid near a barrier have a width L (before instability) of at least twice the Rossby radius $(g'h_1)^{1/2}/f$. Thus bore solutions are not expected to occur. A wedge-like nose forms instead. The observed flow is not blocked and diverted perpendicular to the boundary, and is an entirely laminar flow with Reynolds numbers close to 2×10^2 (based upon the upstream width of the current and the nose velocity). On the other hand, the width of observed stable currents produced by the ring source is as much as eight times the Rossby radius ($F_1^* \approx 60$), and is therefore significantly greater than the pre-

dicted maximum width for a parallel current with (zero) potential vorticity. This difference is probably due to the presence, in the laboratory flows, of non-zero or non-uniform distributions of potential vorticity in each layer, which will allow wider currents to form. The potential vorticity distribution of the current is also important when considering the stability of the flow. Stern's assumption of uniform (or zero) potential vorticity filters out the baroclinic and barotropic modes of instability which require that the gradients of potential vorticity take opposite signs somewhere in the flow, and which successfully explain much of the observed behaviour.

Finally, we can compare our experimental results and theoretical model with oceanic observations. The influence of friction is then based on a vertical eddy viscosity. The East Greenland Current consists of cold, relatively fresh polar water ($T = -1.5°$ C, salinity $S = 34‰$) that flows south over the mately 200 km wide and 200 m deep (Wadhams et al., 1979). With $f = 2\Omega \sin \phi = 1.4 \times 10^{-4}$ s^{-1}, $g' \approx 0.4$ cm s^{-2}, $L \approx 200$ km, $h \approx 200$ m and a total water depth $H \approx 600$ m, the Froude number for the current is $F_1 \approx 10^3$ while $\gamma \approx \frac{1}{2}$. These values imply that the baroclinic instability mechanism will dominate the barotropic instability mechanism. The results of the baroclinic model shown in Fig. 8 predict that, if the current is marginally stable, the most unstable mode has $\lambda \approx L$. The resulting eddies may be expected to have diameters of approximately 100 km, which is twice those observed.

Another buoyancy-driven boundary current on which waves have been observed is the flow of relatively fresh water (originally from the North Atlantic) around the coast of Italy and France in the Ligurian Sea. Wald et al. (1980) report that satellite photographs taken in December 1977 revealed a number of wave-like structures on the edge of this current. They moved in the direction of the current (cyclonic) and had a wavelength of 40 ± 10 km. The Rossby radius of deformation was 7 km and the currrent width 35 km, so that a two-layer approximation gives $F_1 \approx 30$. The upper layer is 100 m deep and, although the depth of the water column is 2000 m, there is significant stratification within the bottom layer. Consequently, the effective depth of the lower layer is considerably less than the total depth of the water column, and we will assume that $\gamma \lesssim 1$. The observed instability is likely to be predominantly baroclinic and the model predicts (Fig. 8) $\lambda \approx 2L \approx 70$ km which, again, is twice that observed.

The third oceanographic example is the Norwegian Coastal Current. This consists of cold, brackish water (2—4° C, 32—35‰) which flows through the Skagerrak from the Baltic and is modified by terrestrial run-off as it flows northward along the west coast of Norway. Measurements in the spring of 1979 (Johannessen and Mork, 1979) showed that the current was 55 ± 10 km wide and that its depth near the coast was 100—150 m. Typical values of F_1 were 30 ± 10, and γ varied from 0.5 to 1. Satellite and other synoptic scale observations revealed that the outer edge of the current undergoes large convolutions which propagate northward and which have a wavelength of

60—100 km. In this case the observed values of $\lambda/L \approx 1$—2 agree reasonably well with the experimental results, although the theoretical model predicts λ/L slightly greater than 2.

A number of features may contribute to this discrepancy between the oceanic observations and the model predictions. The oceanic stratification is only approximately represented by two uniform layers separated by a sharp interface. Density gradients in the layers, and across the transition region, may allow modes of smaller vertical and horizontal scales, which are filtered out of a two-layer model, to become unstable (Pedlosky, 1979). Also, the widths L of the oceanic currents are measured after instability and the width of the laboratory currents is observed to increase dramatically after instability. Since $\lambda \propto L^{1/2}$ for $F_1 >> 1$ (eq. 10), an overestimate of the width would lead to an overestimate in the prediction of the wavelength of the marginally unstable mode.

An alternative explanation of the observed wavelengths may be that the oceanic currents are supercritical rather than marginally unstable. Supercritical instability (in an inviscid fluid) leads to growing modes with $\lambda/L^* \approx 2\pi F_1^{-1/2}\gamma^{-1/4}$ (Griffiths and Linden, 1981), giving $\lambda \approx 45$ km for the East Greenland Current and $\lambda \approx 35$ km for the Ligurian Sea. Those values agree well with the observations. For the Norwegian Coastal Current, supercritical instability (Mysak and Schott, 1977) predicts $\lambda \approx 60$ km which is consistent with the shortest waves observed. It is not clear how such supercritical conditions might be set up in practice, although they may arise from temporal variations in the source strength.

ACKNOWLEDGEMENT

R.W.G. acknowledges the support of a grant from the U.K. Natural Environment Research Council.

REFERENCES

Busse, F.H., 1968. Shear flow instability in rotating systems. J. Fluid Mech., 33: 577—589.

Griffiths, R.W. and Linden, P.F., 1981. The stability of vortices in a rotating, stratified fluid. J. Fluid Mech., 105: 283—316.

Hide, R., 1967. Detached shear layers in a rotating fluid. J. Fluid Mech., 29: 39—60.

Holland, W.R. and Haidvogel, D.B., 1980. A parameter study of the mixed instability of idealized ocean currents. Dyn. Atmos. Oceans, 4: 185—215.

Johannessen, O.M. and Mork, M., 1979. Remote sensing experiment in the Norwegian Coastal Waters. Spring 1979. Rapport 3/79, Geophysisk Institutt, Universitetet i. Bergen.

Jones, S., 1977. Instabilities and wave interactions in a rotating two-layer fluid. PhD thesis, University of Cambridge.

Killworth, P.D., 1980. Barotropic and baroclinic instability in rotating stratified fluids. Dyn. Atmos. Oceans, 4: 143—184.

Mysak, L.A. and Schott, F., 1977. Evidence for baroclinic instability of the Norwegian Current. J. Geophys. Res., 82: 2087—2095.
Pedlosky, J., 1964. The stability of currents in the atmosphere and the ocean. Part I. J. Atmos. Sci., 21: 201—219.
Pedlosky, J., 1970. Finite-amplitude baroclinic waves. J. Atmos. Sci., 27: 15—30.
Pedlosky, J., 1979. Geophysical Fluid Dynamics. Springer-Verlag, New York, NY.
Phillips, N.A., 1954. Energy transformations and meridional circulations associated with simple baroclinic waves in a two-level quasi-geostrophic model. Tellus, 6: 273—286.
Stern, M.E., 1980. Geostrophic fronts, bores, breaking and blocking waves. J. Fluid Mech., 99: 687—704.
Wadhams, P., Gill, A.E. and Linden, P.F., 1979. Transects by submarine of the East Greenland Polar Front. Deep-Sea Res., 26A: 1311—1327.
Wald, L., Crepon, M. and Monget, J.M., 1980. Low-frequency waves in the Ligurian Sea during December 1977 from satellite NOAA 5 (in press).